

Formation and Structural Anomaly of the Metastable Phases in an Immiscible Ag–Mo System Studied by Ion Beam Mixing and Molecular Dynamics Simulation

K. P. Tai, X. D. Dai, Y. X. Shen, and B. X. Liu*

Advanced Materials Laboratory, Department of Materials Science and Engineering, Tsinghua University, Beijing 100084, China

Received: May 30, 2005; In Final Form: November 2, 2005

For the equilibrium immiscible Ag–Mo system characterized by a large positive heat of formation, the nanosized Ag–Mo multilayered samples are designed and prepared to include sufficient interfacial free energy to elevate their initial energetic states to be higher than that of either the amorphous phase or solid solution and then subject to 200 keV xenon ion irradiation. The results show that a uniform amorphous alloy can be obtained within a composition range, at least, from 25 to 88 atom % of Mo. Interestingly, in the intermediate stage of ion irradiation, a bcc phase, an amorphous phase, and an order (bcc)–disorder coexisting state appear simultaneously in the Ag₁₂Mo₈₈ multilayered sample and extend over the entire bright field image with unanimously homogeneous composition. In thermodynamic modeling, a Gibbs free energy diagram of the Ag–Mo system is constructed, based on Miedema's model, and suggests that within a narrow composition regime of 85–90 atom % of Mo, the energy difference between the bcc and the amorphous phases is extremely small, which is probably the very reason for the order–disorder coexisting state to appear. In atomistic modeling, an ab initio derived Ag–Mo potential is applied to perform molecular dynamics simulations. The simulations not only determine an intrinsic glass-forming ability/range (GFA/GFR) of the Ag–Mo system to be from 10 to 88 atom % of Mo but also reveal the possibility of the formation/appearance of a crystalline and amorphous mixture in a narrow composition regime of 88–92 atom % of Mo. Apparently, the theoretical results are in excellent agreement and/or compatible with the experimental observations in ion beam mixing.

1. Introduction

In 1960, Duwez et al. obtained the first amorphous alloy (namely, metallic glass) by using liquid melt quenching to freeze an Au–Si alloy in its liquid state from the melt¹ and the newly discovered state of matter was later defined as amorphous solid.^{2,3} Amorphous alloys are expected to have novel properties in many aspects, and a great effort has been paid, in the past four decades, to the development of nonequilibrium materials processing techniques, which are capable of producing new metastable alloys in either amorphous or crystalline structure and of fabricating an artificial solid-state microstructure.⁴ Although the amorphous alloy was discovered more than 40 years ago, there are still many scientific issues remaining for further studies, especially the theoretical modeling concerning the formation and the structural characteristics of the nonequilibrium alloys. The majority of amorphous alloys produced until now are in easy glass-forming systems exhibiting negative heats of formation (ΔH_f). For many systems with positive ΔH_f values, though some novel behaviors and features have been observed in experiments, theoretical modeling has so far been less studied. In recent years, much interest has been switched to the equilibrium immiscible systems with large positive ΔH_f values focused not only on the formation of but also on revealing the structural characteristics of the synthesized nonequilibrium alloys. For instance, He et al. have studied the amorphization behavior in the immiscible Ag–Ni system with a positive $\Delta H_f = +22$ kJ/mol and claimed that the Ag–Ni amorphous phase was not uniform and somehow of spinodal-like structure.⁵ Guo

et al. have proposed a cage-like atomic arrangement for the amorphous alloys formed in the immiscible Ag–Co system with a positive $\Delta H_f = +26$ kJ/mol.⁶

In synthesizing new nonequilibrium alloys, ion beam mixing (IBM) of multiple metal layers was introduced in the early 1980s, and due to its very powerful capability, IBM has so far produced a variety of nonequilibrium alloys in numerous binary metal systems. In the recent decade, IBM has been focused on studying the binary metal systems characterized by positive ΔH_f values, and some of the systems are essentially immiscible at equilibrium. Concerning the mixing efficiency between the immiscible metals, Cheng has reported that, to increase the mixing efficiency, IBM should proceed at low temperature to minimize the thermal excitation to trigger the repulsive interaction between the immiscible metals.⁷ In practice, decreasing the thickness of the individual layers in the studied metal–metal multilayered films could also help to enhance the mixing efficiency, because the atomic migration length required for intermixing is significantly reduced. In fact, when dealing with the systems with positive ΔH_f values, IBM has been conducted with the metal–metal multilayered films including a large number of layers to enhance the mixing efficiency as well as to include an adequate amount of interfacial free energy for elevating the initial energetic state of the films up to a desired level. For example, Zhang et al. have studied three sets of Y–Mo ($\Delta H_f = +26$ kJ/mol) multilayered films, which include 9, 11, and 19 layers, respectively. The energetically favored Y–Mo metastable phases could be predicted in the Y–Mo system according to the thermodynamic calculations. Interestingly, the results from the properly conducted IBM at room

* To whom correspondence should be addressed. E-mail: dmslxbx@tsinghua.edu.cn.

temperature, with confined ion beam current density, were indeed in excellent agreement with the prediction, for example, Y–Mo amorphous alloys at about equiatomic stoichiometry were only obtained in the Y–Mo multilayered films with 19 layers but not in the other two sets of Y–Mo samples. In the other two sets of samples, the Y–Mo amorphous alloys could only be formed with the compositions either close to the Y side or close to the Mo end.^{8,9} These results clearly demonstrated that the interfacial free energy played an important or decisive role in amorphous alloy formation in the Y–Mo system, while the effects of other possible influencing factors, such as defects, mechanical stress, etc., were minor. In fact, by taking seriously the above-mentioned precautions, IBM has successfully fabricated a number of metastable alloys and/or artificial solid-state microstructures. In other words, IBM conducted in such a way can be named as interface-assisted IBM.¹⁰ Following Zhang's approach, in the studied metal–metal multilayered samples, the individual layer thickness was intentionally designed to be a couple of nanometers, differing considerably from the typical thickness of 5–8 nm in the previously conducted IBM. A very recent example was to use the equilibrium immiscible Ag–W system which has the largest positive ΔH_f value ($= +65$ kJ/mol) among the transition metal alloys, and indeed, amorphous alloys were obtained by interface-assisted IBM.¹¹

In the present study, the Ag–Mo system with the second largest positive ΔH_f value ($= +56$ kJ/mol¹²) is selected to investigate the possibility of producing nonequilibrium alloys by IBM as well as to reveal the structural characteristics of the obtained alloys. Thermodynamic calculation is conducted, based on Miedema's model, to give macroscopic insight concerning the formation of the metastable phases by comparing the relative energetic levels of the competing phases in question. In atomistic modeling, with the aid of ab initio calculations for acquiring some physical data, an n -body potential of the Ag–Mo system is constructed and applied in molecular dynamic (MD) simulations to determine the glass-formation ability/range (GFA/GFR) of the system. A brief discussion is followed to compare the experimental observations from IBM and the theoretical modeling.

2. Experimental Procedure and Theoretical Methods

2.1. Experimental Procedure of Ion Beam Mixing. In the present IBM experiment, three sets of Ag–Mo multilayered samples with overall compositions of Ag₇₅Mo₂₅, Ag₃₅Mo₆₅, and Ag₁₂Mo₈₈, respectively, are designed and 200 keV xenon ions are employed as the irradiating ions. The total thickness of the Ag–Mo multilayered films should be designed to be around 45 nm to match the range of the irradiating ions according to the TRIM program.¹³ The Ag₇₅Mo₂₅, Ag₃₅Mo₆₅, and Ag₁₂Mo₈₈ multilayered films consist of 11, 15 (and 11), and 11 layers (i.e., 10, 14 (and 10), and 10 interfaces), respectively, and the thickness of the individual metal layer is therefore in a range of 3–5 nm. The desired compositions of the films are obtained through adjusting the relative thicknesses of the individual Ag and Mo layers. Concerning the details of the calculation of the interfacial free energy and design of the multilayered films, the readers are referred to some previous publications from the authors' group.⁸ The intrinsic energy difference of various states, that is, between the initial Ag–Mo multilayered films and various metastable Ag–Mo phases, is the major thermodynamic driving force for the related structural phase transformation and ion irradiation is the trigger for intermixing between the Ag and Mo layers, resulting in the formation of the respective metastable Ag–Mo phases. The Ag–Mo multilayered samples

are prepared by depositing alternatively pure Ag (99.9%) and Mo (99.9%) at a rate of 0.5 Å/s onto NaCl single crystals as substrates in an e-gun evaporation system with a vacuum level of 10^{-6} Pa. The as-deposited Ag–Mo samples are then irradiated by xenon ions in an implanter with a vacuum level better than 5×10^{-4} Pa, and the irradiation dose is in a range from 4×10^{14} to 5×10^{15} Xe⁺/cm². During xenon ion irradiation, the sample holder is cooled by liquid nitrogen (77 K) and the xenon ion current density is confined to be about 2 μ A/cm² to minimize an otherwise heating effect. For structural characterization, all the Ag–Mo multilayered samples are removed from the substrates by deionized water and put onto the Cu grids for investigation by room-temperature transmission electron microscopy (TEM) bright field examination and selected area diffraction (SAD) analysis to identify the structures in the films. Energy dispersive spectroscopy (EDS) is also employed to determine the real compositions of the as-deposited films and the resultant alloy phases in the films. In the EDS analysis, the beam spot is about 0.3 μ m, which could be considered the resolution of the measurement, and the measuring error in alloy composition is about 5%.

2.2. Thermodynamic Calculation. Generally, the Gibbs free energy of an alloy phase can be calculated by $\Delta G = \Delta H - T\Delta S$, where ΔH and ΔS are the enthalpy and entropy terms, respectively. As a first approximation, the entropy term for a concentrated solid solution (CSS) and amorphous phase is simply taken as that of an ideal solution, that is, $\Delta S = -R[c_A \ln c_A + c_B \ln c_B]$, where R is the gas constant and c_A and c_B are the atomic concentrations of metals A and B, respectively.

According to Miedema's model and Alonso's method,^{12,14–16} the enthalpy change ΔH is the sum of three terms, namely, $\Delta H = \Delta H^c + \Delta H^e + \Delta H^s$, corresponding to the chemical, elastic, and structural contributions, respectively. The chemical term ΔH^c is closely related to the electron redistribution generated at the boundary for the Wigner–Seitz unit cell when alloying and can be calculated by

$$\Delta H^c = c_A c_B [c_B \bar{\Delta H}_{\text{AinB}}^{\text{inter}} + c_A \bar{\Delta H}_{\text{BinA}}^{\text{inter}}] \quad (1)$$

where $\bar{\Delta H}_{\text{AinB}}^{\text{inter}}$ and $\bar{\Delta H}_{\text{BinA}}^{\text{inter}}$ are the solution enthalpies of A solved in B and that of B solved in A, respectively, and all these values have been compiled by Niessen et al.^{12,14}

The elastic term ΔH^e for a CSS is caused by the atomic size mismatch of the two constituent metals and can be expressed by taking the weighted average of the mismatch energies^{12,14}

$$\Delta H^e = c_A c_B [c_B \bar{\Delta H}_{\text{AinB}}^{\text{elastic}} + c_A \bar{\Delta H}_{\text{BinA}}^{\text{elastic}}] \quad (2)$$

where $\bar{\Delta H}_{\text{AinB}}^{\text{elastic}}$ and $\bar{\Delta H}_{\text{BinA}}^{\text{elastic}}$ are the partial elastic mismatch energies for A solved in B and B solved in A, respectively, and all these values can be found in some published books and/or comprehensive papers.^{12,14}

The structure term ΔH^s is deduced from the lattice stability $E(Z)$ of the bcc, fcc, and hcp structures as a function of the number of valence electrons Z of the metal^{12,14}

$$\Delta H^s = E(Z) - c_A E(Z_B) - c_B E(Z_A) \quad (3)$$

where $E(Z)$, $E(Z_A)$, and $E(Z_B)$ are the lattice stability of the CSS and pure metals A and B, and Z , Z_A , and Z_B are the mean numbers of valence electrons of the CSS and the numbers of valence electrons of pure metals A and B, respectively.^{12,14}

When compared with the CSS, the structural and elastic terms for the formation enthalpy of an amorphous alloy are absent or significantly reduced, that is, $\Delta H^e \approx 0$ and $\Delta H^s \approx 0$.^{17,18} There

TABLE 1: Parameters Used in the Thermodynamic Calculation in the Ag–Mo System

parameter	$\Delta\bar{H}_{\text{AinB}}^{\text{inter}}$ (kJ·mol ⁻¹)	$\Delta\bar{H}_{\text{AinB}}^{\text{elastic}}$ (kJ·mol ⁻¹)	$E(Z_A)$ (kJ·mol ⁻¹)	S_{fA} (10 ⁵ m ²)	$\gamma_{\text{AB}}^{\text{SS}}$ (J·m ⁻²)
Ag			-2.0	2.12	
Mo			-12.0	2.0	
Ag in Mo	153.4	0.84			1.36
Mo in Ag	143.78	2.21			1.4

is, however, apart from the chemical term, another term contributing to the formation enthalpy of the amorphous alloy that reflects the relative disordering and therefore the formation enthalpy of the amorphous alloy can be expressed by^{12,14}

$$\Delta H^{\text{amorphous}} = \Delta H^c + \Delta H^{\text{topological}} \quad (4)$$

where the topological enthalpy $\Delta H^{\text{topological}}$ accounts for the difference between the crystalline and amorphous states, which can be calculated by^{12,14}

$$\Delta H^{\text{topological}} = 3.5(c_A T_{\text{m,A}} + c_B T_{\text{m,B}}) \quad (5)$$

where $T_{\text{m,A}}$ and $T_{\text{m,B}}$ are the melting temperatures of the metals A and B, respectively. Meanwhile, the chemical term of the amorphous alloy ΔH^c can be assumed to be equal to that of the CSS.

For a system with metals A and B, the Gibbs free energy of the initial state of the A–B multilayered samples should be calculated by adding the interfacial free energy to the ground state (i.e., the zero line) representing a mechanical mixture of A and B in the bulk form. According to Zhang et al.,^{8,12,19,20} the excess interfacial free energy of the multilayered samples can be calculated by $\Delta G_{\text{mul}} = \alpha_A S_{\text{fA}} \gamma_{\text{BA}}^{\text{SS}} + \alpha_B S_{\text{fB}} \gamma_{\text{AB}}^{\text{SS}}$, where S_{fA} and S_{fB} are the surface areas occupied by one mole of atoms A and B, respectively, α_A and α_B are the fraction of the interfacial atoms A and B vs the total number of atoms in the A–B multilayered samples, and $\gamma_{\text{AB}}^{\text{SS}}$ (or $\gamma_{\text{BA}}^{\text{SS}}$) are the interfacial free energy of one mole of atoms A (or B) solved in B (or A). These terms can easily be calculated following the well-documented literature.^{8,12,19,20} The parameters used in the thermodynamic calculation are all listed in Table 1.

2.3. Methods of Ab Initio Calculations and of Construction of n -Body Potential. Since we are dealing with the equilibrium immiscible Ag–Mo system, for which there are very few available experimental data related to the Ag–Mo compounds, it is a challenging task to fit the Ag–Mo cross potential. In this respect, the first-principles calculation based on quantum mechanics is known to be a reliable way to acquire some physical properties of the compounds of interest.^{21–23} In the present study, the first-principles calculations are carried out using the well-established Vienna ab initio simulation package (VASP).^{24,25} In the calculation, the plane-wave basis and fully nonlocal Vanderbilt-type ultrasoft pseudo-potentials are employed.²⁶ The exchange and correlation items are described by the generalized-gradient approximation (GGA) proposed by Perdew and Wang.²⁷ The integration in the Brillouin zone is done in a mesh of $11 \times 11 \times 11$ special k points determined according to the so-called Monkhorst–Pack scheme, as such integration is proved to be sufficient for the computation of the simple structures.²⁸ The cutoff energies for Ag and Mo are set to be 249.842 and 224.580 eV, respectively.

The Finnis–Sinclair (FS) formalism based on the second-moment approximation²⁹ is adopted in the present study as a computational framework to construct the n -body potential of the Ag–Mo system. In this regard, though the original FS formalism works very well for many bcc metals, it does not

work well for some fcc metals, especially for the noble metals, which, according to Ackland et al., might be attributed to the electronic structure difference between the bcc and fcc metals.³⁰ Besides, researchers also find that the FS potential is systematically too “soft”, as it moves away from the equilibrium volume.³¹ We, therefore, propose an extension to the original FS formalism for satisfactorily reproducing the physical properties of the fcc metals and enhancing the repulsive interaction between atoms when the potential moves away from the equilibrium position. The proposed potential is therefore named extended-FS potential, in which the total energy of a system, according to the original FS formalism, is given by

$$U_{\text{tot}} = \frac{1}{2} \sum_{ij} V(r_{ij}) - \sum_i [\sum_{j \neq i} A^2 \phi(r_{ij})]^{1/2} \quad (6)$$

The first term in eq 6 is a conventional, central pair-potential summation, which is expressed by a quartic polynomial in the original FS formalism²⁹ and by an exponential form in Johnson’s EAM potential.³² We propose using a polynomial formalism with an important extension by a hexad form to enhance the repulsive interaction between the atoms and the extended term is expressed by

$$V(r) = \begin{cases} (r - c)^2(c_0 + c_1 r + c_2 r^2 + c_3 r^3 + c_4 r^4), & r \leq c \\ 0, & r > c \end{cases} \quad (7)$$

where c is a cutoff parameter assumed to lie between the second and third neighbor atoms. c_0 , c_1 , c_2 , c_3 , and c_4 are the potential parameters to be fitted. The second term in eq 6 is the n -body term. It should be noted that the physical meaning of the electronic density function $\phi(r_{ij})$ for the fcc metals, especially for the fcc noble metals, is quite different from that for the bcc metals. For the bcc metals, the outer electronic structure is a partially filled d-band, whereas for the fcc metals, it is close to or just a full filled d-band, which becomes difficult when the original FS formalism treats the fcc metals, especially the fcc noble metals. To overcome this difficulty, we extend the electronic density function by adding a quartic term to enhance the flexibility as well as improve the precision of the potential and it is expressed by

$$\phi(r) = \begin{cases} (r - d)^2 + B^2(r - d)^4, & r \leq d \\ 0, & r > d \end{cases} \quad (8)$$

Note that the term $B^2(r - d)^4$ is added in eq 8 to improve the performance of the potential in describing the electronic density of the metals, especially of the fcc metals. In eq 8, the cutoff parameter d is also assumed to lie between the second and third neighbor atoms. Apparently, the proposed extended-FS potential is a simple short-range potential, and when the potential parameters, c_3 , c_4 , and B , are all set to be zero, the extended-FS potential turns into the original FS formalism. Consequently, the extended-FS potential could work for whatever the original FS formalism could do for the bcc metals and is expected to work well for the fcc metals as well as for the bcc–fcc alloy systems.

2.4. Molecular Dynamics Simulation and Characterization

Methods. In the present study, the MD simulations are carried out with the Parrinello–Rahman constant pressure scheme and the equations of motion are solved using the second-order four-value predictor-corrector algorithm of Gear with a time step $t = 5 \times 10^{-15}$ s.^{33–35} The constant pressure is set at 0 Pa, and the simulation temperature is set at 300 K. In the simulations, we use the fcc Ag-based and bcc Mo-based solid solutions models,³⁶ respectively. The solid solution models consist of $7 \times 7 \times 7 = 343$ unit cells (1372 atoms) for the fcc Ag-based solid solution and $9 \times 9 \times 9 = 729$ unit cells (1458 atoms) for the bcc Mo-based solid solutions, respectively. For all solid solution models, the [100], [010], and [001] crystalline directions are parallel to the x , y , and z axes, respectively, and in the three axes, the periodic boundary conditions are adopted. In setting the solid solution models, the solute atoms are added into the model by randomly substituting a desired number of solvent atoms to obtain the initial state of the solid solution models. Simulations are conducted for 50 000 to 150 000 MD time steps to reach a relatively stable (i.e., metastable) state, at which all the related dynamic variables show no secular variation.

The structural phase transitions in the solid solutions are monitored by the pair-correlation function $g(r)$, planar structure factor $S(\mathbf{k}, \mathbf{z})$, density profiles of each species along the z direction $\rho_\alpha(z)$, and the projections of atomic positions. As one of the main criteria to determine an amorphous structure, $g(r)$ is commonly used to characterize the structure to be either crystalline or amorphous or disordered. To calculate the pair-correlation function $g(r)$, each atom was imagined to be at the center of a series of concentric spheres. The atomic density $\rho(r)$ was defined to be the number of the atoms in each spherical shell divided by the volume of that shell, with the consideration of those periodic images located outside the block. By averaging over all the atoms within 200 time steps, the $g(r)$ can then be obtained by the following formula

$$g(r) = \frac{\rho(r)}{\rho_0} \quad (9)$$

where $\rho(r)$ denotes the atomic density at $r = |\mathbf{r}|$ and $r = 0$ defines the position of a reference. ρ_0 is an average atomic density in the whole model. The planar structure factor $S(\mathbf{k}, \mathbf{z})$ is a Fourier transformation of the density in each crystallographic plane parallel to an x – y plane and defined by Phillpot et al. Accordingly, it can be expressed as³⁷

$$S(\mathbf{k}, \mathbf{z}) = \left\langle \frac{1}{N_z^2} \left| \sum_{j=1}^{N_z} \exp(i\mathbf{k} \cdot \mathbf{r}_j) \right|^2 \right\rangle \quad (10)$$

where \mathbf{z} labels the crystal plane to which the point \mathbf{r}_j belongs in the initial configuration, and \mathbf{k} is an arbitrary vector of the planar reciprocal lattice. In the present study, $\mathbf{k} = (1, 1)$ is used. N_z is the number of layers perpendicular to the z axis and the square bracket means that $S(\mathbf{k}, \mathbf{z})$ is an average value obtained within some time steps in the MD simulation. Accordingly, the planar structure factor $S = 1$ refers to an entirely ordered crystal, while $S = 0$ is for a completely disordered state. Density profiles $\rho_\alpha(z)$ of each species along the z direction are also calculated to define the position of a single atomic layer, indicating the local (i.e., restricted to the single layer) structural and compositional properties of the models.³⁸

3. Results and Discussion

3.1. Ion Beam Mixing Results. We now present the results of the IBM experiment. The real compositions of the as-

TABLE 2: Structural Phase Transitions in the Ag–Mo Multilayered Samples upon Ion Beam Mixing to Various Ion Doses

alloy system	Ag ₇₅ Mo ₂₅	Ag ₃₅ Mo ₆₅		Ag ₁₂ Mo ₈₈
		11 layers	15 layers	
4×10^{14} Xe ⁺ /cm ²	Ag + Mo	Ag + Mo	Ag + Mo	Ag + Mo
8×10^{14} Xe ⁺ /cm ²	Ag + Mo	Ag + Mo	Ag + Mo	Ag + Mo
1×10^{15} Xe ⁺ /cm ²	A ^a	bcc ^c	A	A + bcc ^e
3×10^{15} Xe ⁺ /cm ²	fcc ^b	bcc	PA ^d + bcc	bcc
5×10^{15} Xe ⁺ /cm ²	fcc	bcc	bcc	A

^a A: completely amorphized. ^b fcc: fcc solid solution. ^c bcc: bcc solid solution. ^d PA: partially amorphized. ^e A + bcc: amorphous and bcc crystalline coexisting.

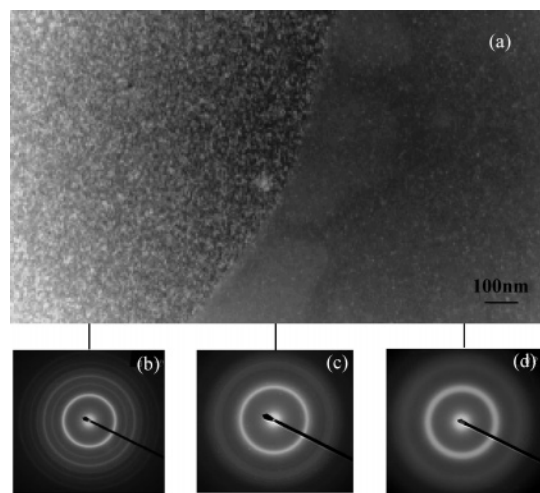


Figure 1. Bright-field image (a) and the corresponding selected area diffraction patterns (b), (c), and (d) of the Ag₁₂Mo₈₈ multilayered sample with 11 layers at an irradiation dose of 1×10^{15} Xe⁺/cm².

deposited Ag–Mo multilayered samples as well as the ion mixed metastable phases in the samples are determined by EDS at various irradiation stages. To present the detailed structural transitions emerged in four sets of Ag–Mo multilayered samples and determine the GFR of the Ag–Mo system, we present all the experimental results for the Ag–Mo multilayered samples, which are irradiated to doses ranging from 4×10^{14} Xe⁺/cm² to 5×10^{15} Xe⁺/cm² in Table 2.

In the Ag₁₂Mo₈₈ multilayered sample, at a dose of 4×10^{14} Xe⁺/cm² to 8×10^{14} Xe⁺/cm², the crystalline Ag and Mo diffraction lines remain. Interestingly, at a dose of 1×10^{15} Xe⁺/cm², three structurally distant states are observed in the sample. Figure 1 shows a bright-field image and three SAD patterns taken at three structurally distinct regions, respectively. From the contrast, one can obviously see that there exist three structurally distinct regions, which, in fact, extend over the entire bright-field image in a scale of a thousand nanometers. The three structurally distinct regions are identified by the corresponding SAD patterns to be a bcc crystalline phase sitting in the left region and a unique amorphous phase in the right region. To the mid-region, a close examination of the corresponding SAD pattern reveals that the second diffused band of weak intensity actually consists of a diffraction ring and a halo, reflected from bcc crystalline and amorphous phases, respectively, indicating an order (bcc)–disorder coexisting state residing between the separated bcc (left region) and amorphous (right region) phases. Moreover, the EDS analyses show that the three structurally distinct regions are unanimously homogeneous in their chemical compositions, as their real compositions are determined to be identical to Ag₁₂Mo₈₈ throughout the entire bright-field image in a span of a thousand nanometers.

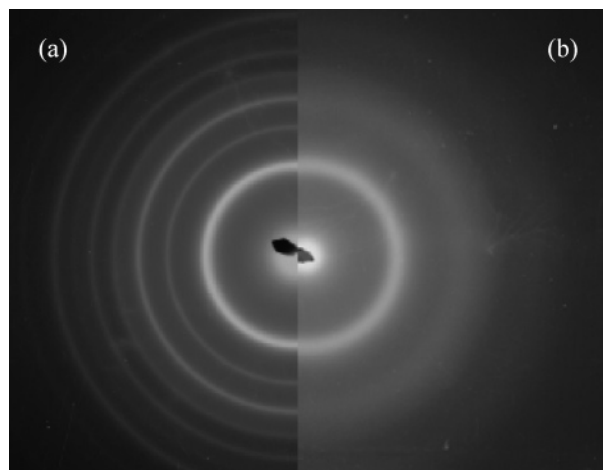


Figure 2. Selected area diffraction patterns for the $\text{Ag}_{12}\text{Mo}_{88}$ multilayered samples with 11 layers (a) the irradiated state at an irradiation dose of $3 \times 10^{15} \text{ Xe}^+/\text{cm}^2$ and (b) a unique amorphous phase formed at an irradiation dose of $5 \times 10^{15} \text{ Xe}^+/\text{cm}^2$.

As mentioned above, the beam spot in EDS analysis is about $0.3 \mu\text{m}$, which is much smaller than the domain sizes of the two resultant phases. In the EDS analysis, the chemical compositions are determined in many randomly chosen local regions of the two resultant phases and the determined values are almost identical within the resolution of the EDS measurement (in practice, we select more than 10 points in each region to determine the real chemical composition, to minimize the statistical as well as the measuring error). By further increasing the irradiation dose to $3 \times 10^{15} \text{ Xe}^+/\text{cm}^2$, the coexisting structure transformed into a uniform bcc supersaturated solid solution (abbreviated as SSSS and hereafter) phase as shown in Figure 2a. More interestingly, at an irradiation dose of $5 \times 10^{15} \text{ Xe}^+/\text{cm}^2$, a unique amorphous phase is formed in the $\text{Ag}_{12}\text{Mo}_{88}$ sample as shown in Figure 2b. The above structural transitions seem to suggest that the bcc SSSS and amorphous phases are very close in their energetic states, and it will be shown later that, according to the thermodynamic calculations, the free energies of the amorphous and metastable bcc phases are indeed very close within a narrow composition region (see Figure 7).

In the $\text{Ag}_{35}\text{Mo}_{65}$ sample with 15 layers, the fcc + bcc crystalline phases remain unchanged within the irradiation doses ranging from $4 \times 10^{14} \text{ Xe}^+/\text{cm}^2$ to $8 \times 10^{14} \text{ Xe}^+/\text{cm}^2$. By increasing the dose up to $1 \times 10^{15} \text{ Xe}^+/\text{cm}^2$, a unique amorphous phase is also obtained as evidenced by the corresponding SAD pattern shown in Figure 3a. By further increasing the irradiation dose up from $3 \times 10^{15} \text{ Xe}^+/\text{cm}^2$ to $5 \times 10^{15} \text{ Xe}^+/\text{cm}^2$, an amorphous-to-crystalline transition took place. Figure 3b exhibits a SAD pattern taken at an irradiation dose of $3 \times 10^{15} \text{ Xe}^+/\text{cm}^2$. It can be seen that the amorphous phase has partially transformed into a bcc SSSS phase, and finally at an irradiation dose of $5 \times 10^{15} \text{ Xe}^+/\text{cm}^2$, the amorphous phase has completely transformed into the bcc SSSS phase. The corresponding bright-field image and SAD pattern are shown in Figure 4. These results imply that the metastable crystalline bcc phase could be relatively stable upon irradiation as long as it was formed. In addition, we have also designed and prepared another $\text{Ag}_{35}\text{Mo}_{65}$ sample with 11 layers, and accordingly, the initial energetic state of the sample was lower than the corresponding amorphous phase (as shown in Figure 7). In the IBM experiment, no amorphization has been observed in the sample up to the presently conducted highest ion dose of $5 \times 10^{15} \text{ Xe}^+/\text{cm}^2$ as shown in Table 2, lending further support to the validity of the thermodynamic modeling.

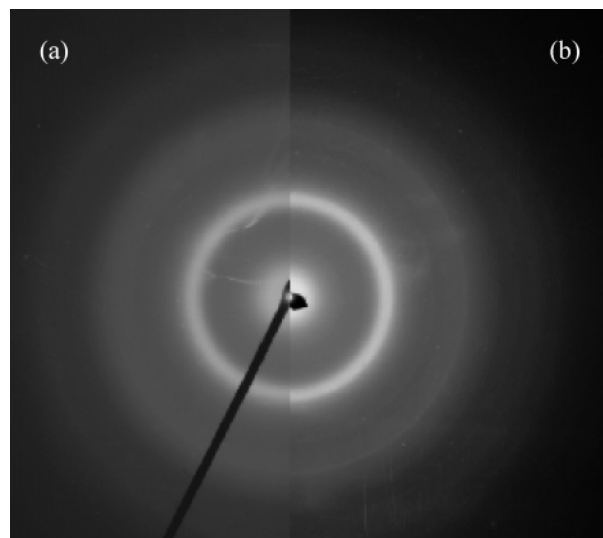


Figure 3. Selected area diffraction patterns for the $\text{Ag}_{35}\text{Mo}_{65}$ multilayered samples with 15 layers (a) a unique amorphous phase formed at an irradiation dose of $1 \times 10^{15} \text{ Xe}^+/\text{cm}^2$ and (b) the irradiated state at an irradiation dose of $3 \times 10^{15} \text{ Xe}^+/\text{cm}^2$.

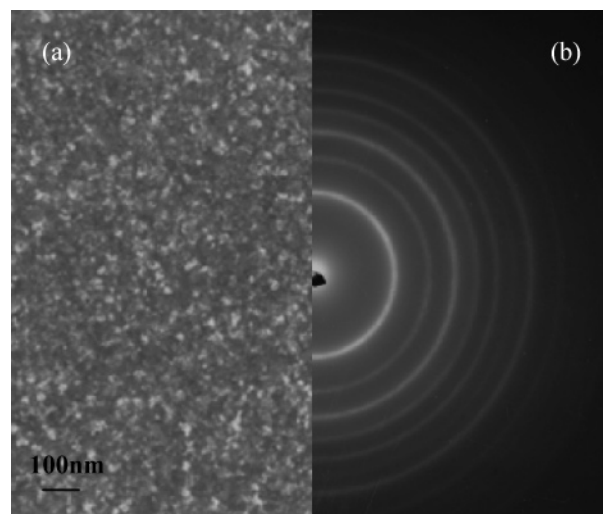


Figure 4. Bright-field image (a) and selected area diffraction pattern (b) for the $\text{Ag}_{35}\text{Mo}_{65}$ multilayered sample with 15 layers at an irradiation dose of $5 \times 10^{15} \text{ Xe}^+/\text{cm}^2$.

For the $\text{Ag}_{75}\text{Mo}_{25}$ multilayered sample, Figure 5a shows a SAD pattern taken at an irradiation dose of $8 \times 10^{14} \text{ Xe}^+/\text{cm}^2$, and from Figure 5a, one can clearly see the sharp diffraction rings, which can be indexed to be from an fcc Ag and a bcc Mo. Figure 5b shows the SAD pattern and the bright-field image taken at an irradiation dose of $1 \times 10^{15} \text{ Xe}^+/\text{cm}^2$, and from Figure 5b, one can see that the sharp diffraction lines disappeared and transformed into diffused halos, indicating that a unique amorphous phase is formed. When the irradiation dose is increased up to $3 \times 10^{15} \text{ Xe}^+/\text{cm}^2$ and further to $5 \times 10^{15} \text{ Xe}^+/\text{cm}^2$, a uniform Ag-rich fcc SSSS phase is observed. The TEM bright-field image and corresponding SAD pattern are shown in Figure 6. These results mean that the metastable crystalline fcc phase is irradiation hard as long as it is formed.

From the experimental results listed in Table 2, one sees clearly that the amorphous phase can be formed within the composition range of 25–88 atom % of Mo, which can be considered as the experimentally determined GFA/GFR of the Ag–Mo system.

3.2. Thermodynamic Modeling. We first construct a Gibbs free energy diagram of the Ag–Mo system by calculating the

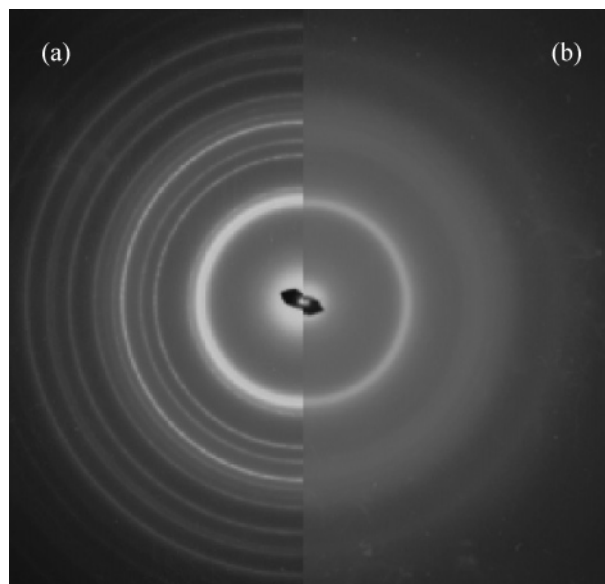


Figure 5. Selected area diffraction patterns for the Ag₇₅Mo₂₅ multilayered samples with 11 layers (a) the irradiated state at an irradiation dose of 8×10^{14} Xe⁺/cm² and (b) a unique amorphous phase formed at an irradiation dose of 1×10^{15} Xe⁺/cm².

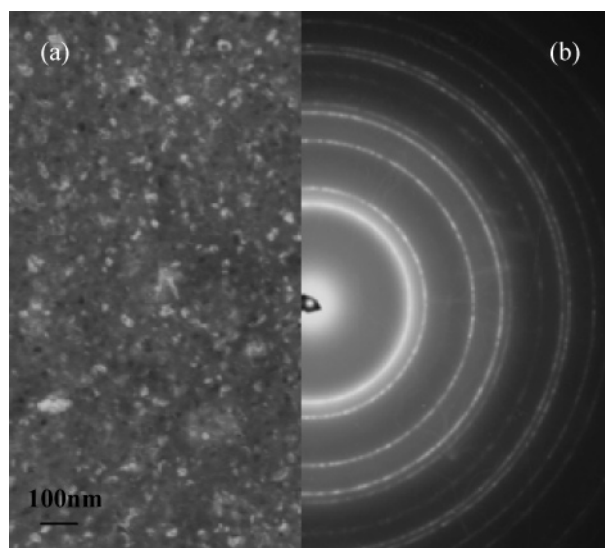


Figure 6. Bright-field image (a) and selected area diffraction pattern (b) for the Ag₇₅Mo₂₅ multilayered sample with 11 layers at an irradiation dose of 5×10^{15} Xe⁺/cm.

free energy curves of all the alloy phases in question, by using Miedema's model¹² and Alonso's method.¹⁴ Figure 7 shows the calculated Gibbs free energy diagram, in which the energetic states of the Ag–Mo multilayered films containing 11 and 15 layers are also included to show the energetic sequence of the initial energetic state of the Ag–Mo multilayered films with the various possible metastable states/phases. From the diagram, one sees that the free energy curve of the amorphous phase is convex like in other systems with large, positive ΔH_f values and the free energy of the initial multilayered samples are higher than that of the corresponding solid solutions. Within the composition range less than 25 atom % Mo or higher than 83 atom % Mo (11 layers), the initial energetic state of the multilayered films containing 10 interfaces is higher than the corresponding solid solution and the amorphous phases, which are therefore thermodynamically favored to be formed. By further increasing the interfaces to elevate the initial energetic state to a higher level, it is possible to form these phases over

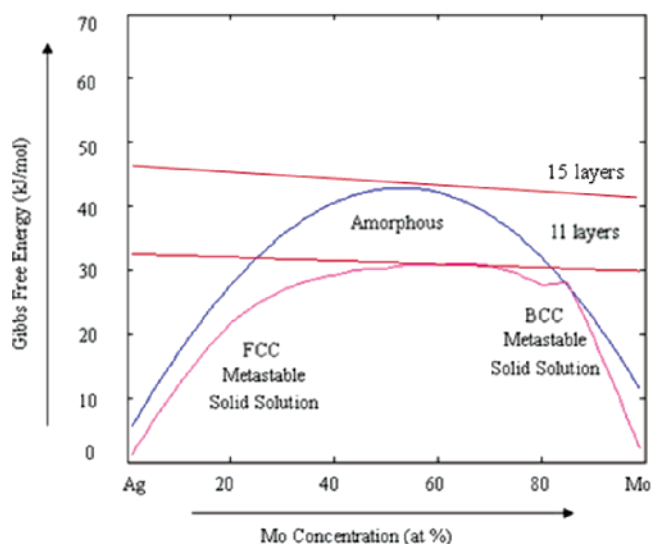


Figure 7. Calculated Gibbs free energy diagram of the Ag–Mo system.

TABLE 3: Fitted Parameters of the n -Body Potentials for the Ag–Mo System

	Ag–Ag	Mo–Mo	Ag–Mo
A (eV·Å ⁻¹)	0.325514	1.848648	0.625749
d (Å)	4.41	4.1472	4.20
c (Å)	4.76	3.2572	4.50
c_0 (eV·Å ⁻²)	10.681200	47.980660	44.406810
c_1 (eV·Å ⁻³)	-12.045170	-34.099240	-45.490260
c_2 (eV·Å ⁻⁴)	5.203072	5.832293	15.605110
c_3 (eV·Å ⁻⁵)	-1.013304	0.101749	-1.793704
c_4 (eV·Å ⁻⁶)	0.0742308	0.0203934	0.0
B (Å ⁻²)	-1.293394	0.0	0.0

TABLE 4: Comparison between Some Calculated Physical Properties Reproduced by the n -body Potentials and the Experimental Values Used in Fitting the Potentials for Pure Ag and Mo

	Ag		Mo	
	experimental	calculated	experimental	calculated
E_c (eV)	2.95 ^a	2.950	6.82 ^c	6.818
a (Å)	4.09 ^a	4.090	3.1472 ^c	3.1472
C_{11} (Mbar)	1.24 ^a	1.240	4.637 ^c	4.631
C_{12} (Mbar)	0.937 ^a	0.937	1.578 ^c	1.589
C_{44} (Mbar)	0.461 ^a	0.461	1.092 ^c	1.087
E_v^f (eV)	1.1 ^b	1.100	3.10 ^d	2.555

^a Reference 39. ^b Reference 40. ^c Reference 41. ^d Reference 42.

a broad composition range, if not forming any terminal solid solutions. (The maximum solid solubility of Mo atoms in Ag almost equals zero and vice versa at 300 K.) Interestingly, within a narrow composition range of 85–90 atom % of Mo, the free energies of the amorphous and metastable bcc phases are almost identical, though the bcc phase has a slightly lower free energy than its amorphous counterpart.

3.3. Construction of an n -Body Ag–Mo Potential. For pure Ag and Mo, the potential parameters are determined by fitting the experimental data, that is, cohesive energy (E_c), lattice constant (a), elastic constants (C_{11} , C_{12} , and C_{44}) as well as vacancy formation energies (E_v^f), and the fitted potential parameters are listed in Table 3. The procedure of parametrization is similar to that described by Finnis and Sinclair.²⁷ The physical properties reproduced from the derived Ag and Mo potentials and the corresponding experimental data used in fitting the potential are listed in Table 4. From Table 4, one can see that the derived Ag and Mo potentials work fairly well in

TABLE 5: Comparison between Some Calculated Physical Properties Reproduced by *ab initio* Calculations and the Experimental Data for Pure Ag and Mo

	Ag		Mo	
	experimental	<i>ab initio</i>	experimental	<i>ab initio</i>
E_c (eV)	2.95 ^a	2.73	6.82 ^b	6.28
a (Å)	4.09 ^a	4.11	3.1472 ^b	3.15

^a Reference 39. ^b Reference 41.**TABLE 6: Comparison of the Cohesive Energy E_c (eV) and Lattice Constant a (Å) Derived from the Constructed Ag–Mo Potential vs Those from *ab initio* Calculations^a**

system	structure	<i>ab initio</i> calculation		present study	
Ag ₃ Mo	L1 ₂	$E_c = 4.13^*$	$a = 3.1166^*$	$E_c = 4.13$	$a = 3.1166$
AgMo	B2	$E_c = 3.23^*$	$a = 3.9161^*$	$E_c = 3.23$	$a = 3.9161$
AgMo ₃	L1 ₂	$E_c = 3.99$	$a = 5.2072$	$E_c = 3.99$	$a = 5.4438$

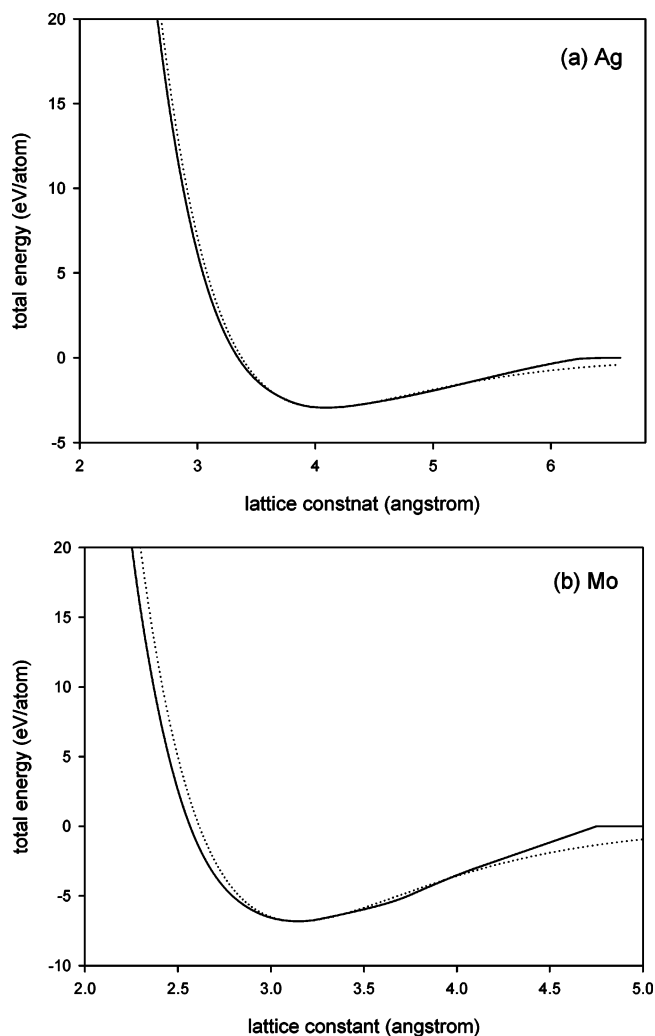
^a The data used in fitting are denoted by asterisks.**TABLE 7: Calculated Lattice Constants a and Cohesive Energies E_c of Pure Ag and Mo in Three Simple Crystalline Structures (fcc, hcp, and bcc)**

structure	Ag		Mo	
	a (Å)	E_c (eV)	a (Å)	E_c (eV)
fcc	4.090	2.950	3.9052	6.563
hcp	2.892	2.949	2.7612	6.562
bcc	3.305	2.908	3.1472	6.820

reproducing some physical properties of the pure Ag and Mo, respectively.

To validate the Vienna *ab initio* simulation package, namely, VASP, we have applied it to calculate the lattice constants and cohesive energies for pure Ag and Mo and compared the calculated results with the experimental values. The comparison is shown in Table 5, and one sees from the table that the *ab initio* calculated results are quite compatible with the experimental data, confirming the validity of the VASP program in calculating some basic physical properties of the metals. Employing the VASP program, we have calculated the lattice constants and cohesive energies for some hypohetic Ag–Mo compounds, and the calculated results are listed in Table 6. With the calculated cohesive energies and lattice constants of the L1₂ Ag₃Mo and B2 AgMo compounds, the cross potential of the Ag–Mo system can be fitted, and the fitted parameters are also listed in Table 3.

To prove the relevance of the Ag and Mo potentials, we first reproduce the cohesive energies, lattice constants of the equilibrium structures, and their metastable structures for pure Ag and Mo, respectively. The calculated results are listed in Table 7. From Table 7, one can clearly see that the cohesive energy of fcc Ag is greater than that of bcc or hcp Ag and that the cohesive energy of bcc Mo is greater than that of the fcc or hcp Mo, reflecting well the fact that the equilibrium states of the pure Ag and Mo are fcc and bcc structures, respectively. In addition, we also compare the equation of state reproduced by the constructed potentials with Rose's equation, which is considered as a universal equation of state for metals.⁴³ It turns out that they are in good agreement as shown in Figure 8. Especially, the equation of state of Ag is quite close to Rose's equation even far from the equilibrium position, indicating that the extended-FS potential can overcome the "soft" phenomenon from the original FS formalism. It is commonly recognized that correctly predicting the basic thermodynamic properties of metals is another important aspect for a relevant *n*-body potential, we therefore validate the pure Ag and Mo potentials

**Figure 8.** Equation of state reproduced from the constructed Ag–Mo potential (solid line) compared with Rose's equation (dashed line).**TABLE 8: Melting Points and Melting Heats for Pure Ag and Mo**

	melting point (K)		melting heat (kJ/mol)	
	experimental ^a	MD simulation	experimental	MD simulation
Ag	1235	1175	11.30	8.95
Mo	2890	3150	32.0	34.64

^a The experimental data are from ref 39.

by reproducing the melting points of Ag and Mo metals from the respective potentials. On the basis of the newly constructed potentials, MD simulations are carried out with the simulation models set in fcc Ag and bcc Mo, respectively, to determine the melting points of the metals.⁴⁴ The knowledge from phase transition theory shows that at the melting point, the heat of formation has an apparent change, which corresponds to the defined melting heat. Accordingly, during the MD simulations, the heat of formation of the simulation model is monitored with variation of temperature to determine the melting point of the metal. The melting points and the melting heats determined by MD simulations as well as the corresponding experimental values for pure Ag and Mo metals are all listed in Table 8. One sees from the table that the calculated melting points and melting heats from the constructed potentials are in good agreement with the experimental values, suggesting that the Ag and Mo potentials are quite relevant to reflect the thermodynamic behavior of the metals.

TABLE 9: Elastic Constants (GPa) of Some Possible Ag–Mo Alloys^a

alloy	structure	C_{11}	C_{12}	C_{13}	C_{33}	C_{44}	C'
Ag ₃ Mo	L1 ₂	121.205	122.396			26.671	−0.596
		3.377	76.052			45.636	−36.337
Ag ₃ Mo	D0 ₃	136.070	133.198			91.645	1.436
		50.045	48.544			14.720	0.750
AgMo ₃	D0 ₁₉	246.802	137.070	130.489	353.670	64.476	54.866
		174.946	82.032	51.030	200.297	14.359	46.456

^a The properties in the upper rows are from first-principles calculations using the CASTEP program, and those in the lower rows are from the constructed Ag–Mo potential.

To test the cross Ag–Mo potential, we employ the potential to reproduce the cohesive energies and the lattice constants of the metastable Ag₃Mo, AgMo, and AgMo₃ compounds, and the results are also listed in Table 6. In the table, the asterisks denote the values used in fitting the potential. One sees that the calculated properties from the constructed cross potential are in good agreement with those obtained from ab initio calculations. Furthermore, based on the constructed Ag–Mo potential, we reproduce the elastic constants of some Ag–Mo alloys at a few specific compositions. For comparison, the well-established ab initio calculation program, that is, CASTEP,⁴⁵ is also employed to acquire the elastic constants. In Table 9, the elastic constants calculated by the Ag–Mo potential and from CASTEP, respectively, are listed. From the table, one sees that the signs, that is, positive or negative, of the derived elastic constants by the potential and from CASTEP are all the same and that there are some unusual features in the elastic behavior of the Ag–Mo system. First, the elastic constants $C' = (C_{11} - C_{12})/2$ of L1₂ Ag₃Mo are negative, implying that the structure is dynamically unstable under an elastic shearing. Second, in all the other cases, the C_{44} and C' values are all positive, suggesting that these structures may elastically be stable. In general, although there are a few cases showing some differences in the calculated elastic constants listed in the table, the agreement between the reproduced values from the constructed Ag–Mo potential and those from CASTEP calculations is reasonably good, suggesting that the Ag–Mo potential is able to reflect the elastic behavior of the Ag–Mo system. It is thus concluded that the constructed Ag–Mo potential is of relevance in describing the atomic interactions in the equilibrium immiscible Ag–Mo system.

3.4. Molecular Dynamic Simulations. We now present the simulation results for the fcc Ag-based solid solution models first. Figure 9 displays the projections of atomic positions for the Ag₉₅Mo₅, Ag₉₀Mo₁₀, and Ag₅₀Mo₅₀ fcc solid solutions upon annealing at 300 K for 120 000 MD time steps, respectively. From the figure, one sees vividly that for the solid solution with 5 atom % of Mo, the fcc structure can clearly be visualized, that is, it still remains in its original crystalline structure. While for the solid solution with solute Mo equal to or greater than 10 atom %, the projection of atomic positions is obviously disordered, indicating that the crystal lattice has collapsed and turned into amorphous, that is, a crystal-to-amorphous transition has taken place. Figure 10 shows the corresponding density profiles $\rho_{\alpha}(z)$ for the solid solutions with the alloy compositions of Ag₉₅Mo₅, Ag₉₀Mo₁₀, and Ag₅₀Mo₅₀, respectively. It can be seen that when the solute concentration is less than 10 atom % Mo, the atomic planes can clearly be distinguished from the density profiles, however, once the Mo concentration equals or exceeds 10 atom %, a relatively uniform distributed density profile appears. To have firm evidence, the total and partial pair-correlation functions $g(r)$ for fcc Ag-based solid solutions are calculated and shown in Figure 11. In the figure, as the $g(r)$ curve of the Ag₉₅Mo₅ simulation model contains apparent sharp peaks even at a large distance r , the Ag₉₅Mo₅ simulation model

is considered to still be in a crystalline structure. In comparison, for the Ag₉₀Mo₁₀ and Ag₅₀Mo₅₀ simulation models, though the first peaks and the second peaks of the $g(r)$ curves are still clear, there are no discernible peaks beyond the third-nearest neighbors. In this regard, Zallen has pointed out in a classic work that the short-range order of an amorphous phase is characterized by the clear first and second nearest neighbor peaks in the radial distribution function (RDF) and discernible peaks in the RDF rarely occur beyond third-nearest neighbors.² Following Zallen's criterion, one can conclude from the calculated total and partial pair-correlation functions (shown by Figure 11) that a crystal-to-amorphous transition has indeed taken place in both the Ag₉₀Mo₁₀ and Ag₅₀Mo₅₀ simulation models. These results clearly indicate that in the Ag–Mo system, when the Mo concentration equals or exceeds 10 atom %, the fcc Ag-based solid solution becomes unstable and turns into an amorphous state. In other words, for the fcc Ag-based solid solution, the critical solid solubility is 10 atom % of Mo, beyond which, the solid solution prefers to transform into an amorphous state.

Similarly, for the bcc Mo-based solid solution, the critical solid solubility is determined to be 88 atom % of Mo. Using the Ag₁₂Mo₈₈ and Ag₇Mo₉₄ solid solution models as examples, Figure 11 also displays their calculated $g(r)$ curves. Apparently, the $g(r)$ curves feature as bcc crystalline structure when the Ag concentration is less than 12 atom %, whereas when the Ag concentration exceeds the critical solid solubility, the $g(r)$ curves are typical of an amorphous structure. For the Ag₁₂Mo₈₈ solid solution models, we also calculated the atomic projections and the density profiles $\rho_{\alpha}(z)$ of the Ag and Mo atoms along the z direction and the calculated results all confirm that the super-saturated solid solution would collapse and turn into a disordered state when the concentration of Ag reaches or exceeds about 12 atom %.

The above simulation results apparently clarify that the origin of the crystal-to-amorphous transition is the collapse of the crystalline lattice, while the solute atoms are exceeding its critical solid solubility. In addition, the simulations determine the two critical solid solubilities of the Ag–Mo system to be 10 atom % of Mo for fcc Ag-based solid solution and 12 atom % of Ag for bcc Mo-based solid solution, respectively. It follows that an amorphous alloy would be formed, when its composition falls in the composition range bound by the two determined critical solid solubilities, thus suggesting that the GFA/GFR of the Ag–Mo system is within 10–88 atom % of Mo. It should be noted that the GFA/GFR is determined directly from the Ag–Mo potential through MD simulations and is therefore an intrinsic property of the system, which could be named as intrinsic GFA/GFR of the Ag–Mo system. In fact, the intrinsic GFA/GFR stands for a maximum composition range, in which an amorphous phase is energetically favored to be formed comparing with its solid solution counterpart. In comparison, the GFA/GFR of a system measured in experiments by using

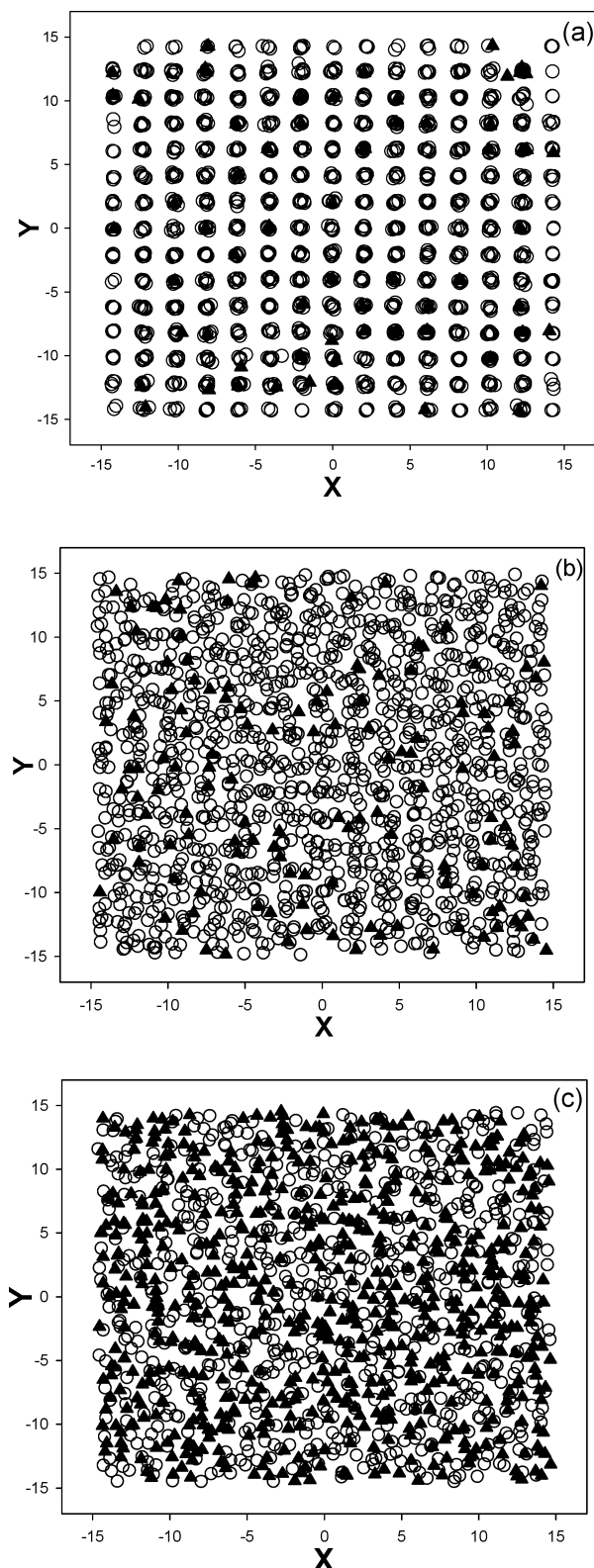


Figure 9. Projections of atomic positions for the (a) $\text{Ag}_{95}\text{Mo}_5$, (b) $\text{Ag}_{90}\text{Mo}_{10}$, and (c) $\text{Ag}_{50}\text{Mo}_{50}$ fcc solid solutions upon annealing at 300 K for 120 000 MD time steps, respectively. Open circles: Ag. Filled triangles: Mo.

any glass-producing technique should be named as nominal GFA/GFR, which is related or limited to the practically applied glass-producing technique. It follows that an intrinsic GFA/GFR of a system is frequently broader than any practically measured nominal GFA/GFR.^{36,46} For example, liquid melt quenching is not able to co-melt the Ag and Mo metals together and therefore

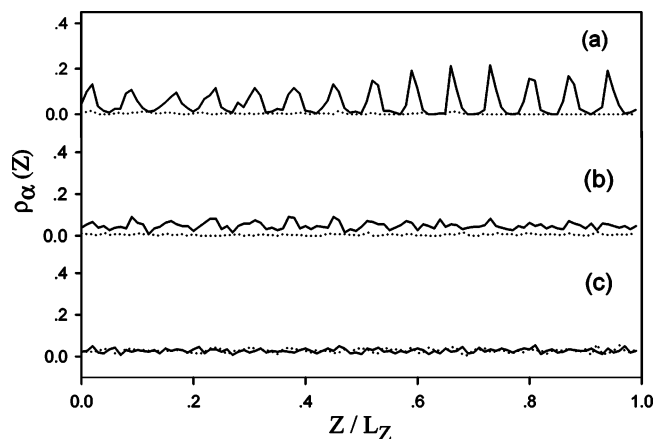


Figure 10. Calculated density profiles $\rho_\alpha(z)$ of the Ag and Mo atoms along the z direction in (a) $\text{Ag}_{95}\text{Mo}_5$, (b) $\text{Ag}_{90}\text{Mo}_{10}$, and (c) $\text{Ag}_{50}\text{Mo}_{50}$ fcc solid solutions upon annealing at 300 K for 120 000 MD time steps, respectively. The solid line is for $\rho_{\text{Ag}}(z)$. The dotted line is for $\rho_{\text{Mo}}(z)$. The ordinate is in arbitrary units.

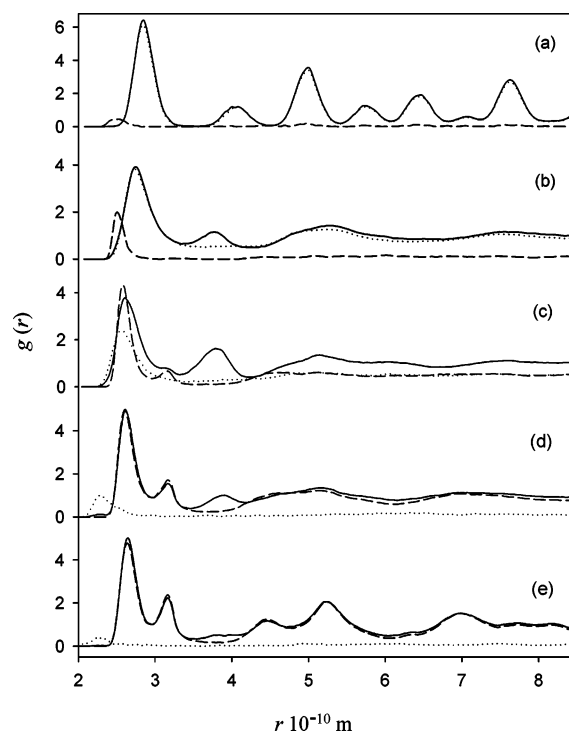


Figure 11. Total and partial pair-correlation functions for the fcc Ag-rich solid solutions upon annealing at 300 K for 120 000 MD time steps. The compositions of the solid solutions are (a) 5 atom %, (b) 10 atom %, and (c) 50 atom % of Mo, respectively. The solid line is for the total $g(r)$, the short dashed line is for the Mo–Mo partial $g(r)$, and the dotted line is for the Ag–Ag partial $g(r)$.

is not able to produce any Ag–Mo amorphous alloy either, suggesting that the GFA/GFR is zero. However, the above results show that ion beam mixing is able to obtain Ag–Mo amorphous alloys in a specific composition range, which is found to be within 25–88 atom % of Mo. As the nominal GFA/GFR (25–88 atom % of Mo) determined in ion beam mixing experiments falls in the intrinsic GFA/GFR (10–88 atom % of Mo) of the Ag–Mo system, it is concluded that the simulation results are fairly compatible with the experimental observations.

More interestingly, the results of MD simulations also show that an order–disorder coexisting state, which has been observed in the above ion beam mixing experiments, does appear within a narrow composition range from 88 to 92 atom % of Mo. Figure 12 shows a projection of atomic positions for the Ag_{10} –

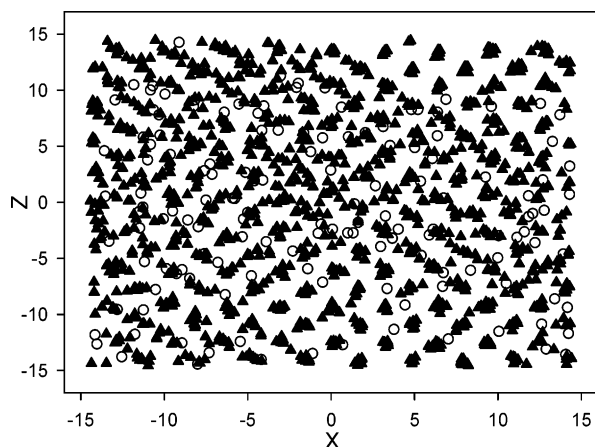


Figure 12. Projection of atomic positions for the $\text{Ag}_{10}\text{Mo}_{90}$ solid solutions upon annealing at 300 K for 55 000 MD time steps. Open circles: Ag. Filled triangles: Mo.

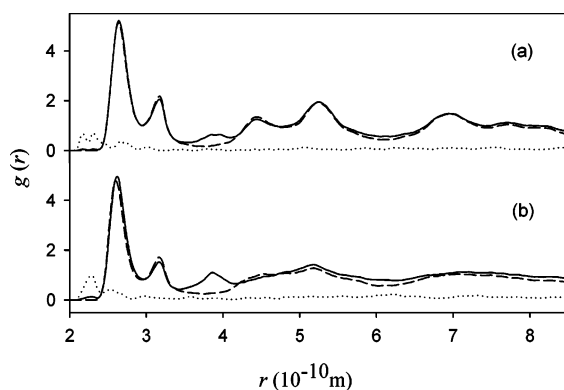


Figure 13. Total and partial pair-correlation functions for (a) nos. 1–4 atomic planes and (b) nos. 9–12 atomic planes in the $\text{Ag}_{10}\text{Mo}_{90}$ solid solution upon annealing at 300 K for 55 000 MD time steps. The solid line is for the total $g(r)$, the dotted line is for the Ag–Ag partial $g(r)$, and the short dashed line is for the Mo–Mo partial $g(r)$.

Mo_{90} solid solution model upon annealing at 300 K for 55 000 MD time steps, beyond which all the related dynamic variables show no secular variation. From Figure 12, one can clearly see that a disorder state has been formed and grown greatly, however some crystalline structure still remains. To further confirm the order–disorder coexisting state, Figure 13 shows the calculated $g(r)$ for nos. 1–4 atomic planes and nos. 9–12 atomic planes in the $\text{Ag}_{10}\text{Mo}_{90}$ solid solution, respectively, upon annealing at 300 K for 55 000 MD time steps. One sees clearly that, in Figure 13a, the shapes of the peaks of the calculated $g(r)$ obviously indicate a crystalline (i.e., order) structure of this local region and that, in Figure 13b, the peaks of the calculated $g(r)$ become weak and even disappear beyond the third-nearest neighbors, indicating that a crystal-to-amorphous transition has taken place in this local region and therefore this local region has become disordered. It is worthwhile to mention that an additional 40 000 MD time steps annealing at 300 K did not result in a visible change in the atomic configuration and in the pair-correlation function either, confirming the possible existence of an order–disorder coexisting state in the Ag–Mo system.

3.5. Discussion. We now discuss further the observations in the $\text{Ag}_{12}\text{Mo}_{88}$ sample, in which not only a unique amorphous phase, a bcc SSSS phase, but also three structurally distinct phases are observed at different irradiation stages. Referring again to Figure 7, one sees that the free energy of the bcc phase is only slightly lower than that of the amorphous phase around the composition of $\text{Ag}_{12}\text{Mo}_{88}$, meaning that the energy difference

between the bcc and amorphous phases is extremely small. In other words, from an energetic point of view, the situation is favored for either bcc or amorphous phase to be formed during the so-called relaxation period in IBM,⁴⁴ and under some specific condition, the amorphous phase may transform into the bcc phase. Interestingly, the amorphous-to-bcc transformation is indeed observed in the above irradiated $\text{Ag}_{12}\text{Mo}_{88}$ sample after room-temperature aging for about five months, that is, the bcc phase overspreads a little bit and the order–disorder coexisting region advances a little into the amorphous region. According to the atomic collision theory,⁴⁶ the process of the three structurally distant states simultaneously appearing is thought to occur as follows: initially, a sequence of ballistic collision is triggered in the Ag–Mo multilayered films by 200 keV xenon ions and is responsible for intermixing of the Ag and Mo layers. At an adequate dose (e.g., $1 \times 10^{15} \text{ Xe}^+/\text{cm}^2$ in this study), uniform mixing is achieved and the mixture of the Ag and Mo atoms is most likely in a highly energetic disordered state. Since the mixing process is a highly dynamic, one involving a large number of atoms in violent motion, there should appear some compositional as well as local atomic configuration fluctuation in the Ag–Mo atomic mixture. When the atomic collision cascade is terminated, the highly energetic state has to relax toward equilibrium. However, because the relaxation period is extremely short, that is, lasting for 10^{-10} s , only a very minor atomic rearrangement could take place. Consequently, either simple structured crystalline phases, such as fcc, bcc, and hcp, may be formed or the disordered structure prefers to preserve, thus forming an amorphous phase. From the above description of the basic process of IBM, one can see that, in the $\text{Ag}_{12}\text{Mo}_{88}$ sample, after irradiation to a dose of $1 \times 10^{15} \text{ Xe}^+/\text{cm}^2$, intermixing is achieved and the Ag–Mo atoms are in a highly energetic, disordered state, they would relax down to the available intermediate states to lower the free energy. Since the phase synthesized by IBM is through a solid–solid transition, the structural compatibility between the newly formed phase and the matrix frequently plays an important role in determining whether the new phase can grow or not, namely, the newly formed phase has the heredity of the matrix. In the present study, we observed the coexisting phenomenon of a bcc metastable crystalline (on the left) and amorphous phase (on the right). Actually, at the termination of the first step of IBM (atomic collision cascade), a mixture of Ag and Mo atoms is obtained, and in the mixture, due to the fluctuation of local atomic configuration (the compositional fluctuation is minor and undetectable by EDS analyses) in the left region, the atomic configuration is close and favored by the crystalline phase, which is formed during the later relaxation step, whereas in the right region, the atomic configuration is close and favored by the disordered phase and an amorphous phase is formed during the later relaxation step. To the mid-region, both atom configurations close and favored by crystalline and disordered phases exist and therefore mixed phases are formed during the relaxation. Therefore, from the kinetic point of view, the coexisting state derives from the fluctuation of the local atomic configuration in the Ag and Mo atomic mixture (with identical chemical composition) achieved at the termination of the atomic collision cascade. As mentioned above, in thermodynamics, both bcc SSSS and the corresponding amorphous phases have about the same opportunity to be formed within a very narrow composition regime, that is, 85–90 atom % of Mo, and therefore, under a suitable dynamic condition in IBM experiments, they could be formed at the same time, which in fact, has been observed in experiments.

In summary, an order–disorder coexisting state is predicted for the highly immiscible Ag–Mo system by MD simulations based on a newly obtained ab initio derived Ag–Mo potential and is observed in an ion beam mixing experiment. Besides, the back-and-forth transformation between bcc SSSS and amorphous phase at irradiation doses from $3 \times 10^{15} \text{ Xe}^+/\text{cm}^2$ to $5 \times 10^{15} \text{ Xe}^+/\text{cm}^2$ (shown in Figure 2) could serve as evidence confirming an extremely small difference in free energy between the BCC and amorphous phases, deduced from the thermodynamic calculation.

Comparing the theoretical GFR predicted by theoretical modeling with the experimental GFR, we find that the experimentally measured GFR being 25 atom % of Mo to 88 atom % of Mo is a little narrower than the calculated GFR from thermodynamic calculation and MD simulations (10–88 atom % of Mo), respectively. However, it is quite reasonable, because, in general, two GFRs deduced from theoretical modeling predict the maximum possible GFRs. Our experimentally measured GFR at a low Mo concentration limit is at 25 atom % of Mo, which is higher than theoretical values obtained in the present study. This is because in ion beam mixing experiments only the alloy compositions of 25 atom % of Mo and higher were studied and the alloy compositions lower than 25 atom % of Mo may need to be examined further. Besides, the experimentally measured GFR at high Mo concentration is 88 atom % of Mo, which is found to be in quite excellent agreement with that determined by the MD simulations.

We now discuss the possible mechanism responsible for the formation of the amorphous phases in the Ag–Mo multilayered samples. As described by the thermodynamic calculations, the Gibbs free energy of the amorphous phase is lower than the corresponding initial multilayered samples as indicated in Figure 7, meaning that the amorphous phase may be formed and indeed obtained by IBM. In the present study, the atomic collision cascade was responsible for inducing the interfacial diffusion of Mo atoms into its partner Ag lattices and vice versa, resulting in forming a highly energetic Ag–Mo mixture. During the relaxation, the effective cooling rate available in IBM can be as high as 10^{13-14} K/s .⁴⁷ Under such a high cooling rate, the mixture is not allowed to proceed directly to an equilibrium state in most cases and often resides at some intermediate state which allows only a limited rearrangement of the atoms. In addition, the very short time of relaxation prevents the nucleation and growth processes of a phase of complicated structure, as long-range diffusion is impossible. From the viewpoint of atomic mobility, the present MD simulations can also reveal the physical mechanism of amorphous formation vividly, that is, when the amount of the Mo atoms in the Ag lattice reached values beyond maximal solid solubility (i.e., 10 atom % Mo), the crystalline lattice collapsed and became a disordered amorphous phase.

Additionally, within the studied composition range, the corresponding fcc/bcc SSSS was also obtained in the amorphous-to-crystalline process and the transformation mechanism is discussed as follows. From thermodynamic calculations shown in Figure 7, prior to forming an fcc/bcc SSSS, an amorphous phase may first be obtained because the amorphous phase has a higher energy than that of the fcc/bcc SSSS phase. Consequently, from a kinetic point of view, during the first step of atomic collision cascade, the lower irradiation dose (about $1 \times 10^{15} \text{ Xe}^+/\text{cm}^2$) was mainly responsible for the formation of the amorphous phases, while the higher irradiation dose (up to $5 \times 10^{15} \text{ Xe}^+/\text{cm}^2$) was responsible for the rearrangement of the uniform mixing disordered state to a crystalline phase which

has a lower free energy. From the $\text{Ag}_{35}\text{Mo}_{65}$ multilayered sample, one can obviously observe the formation sequence at the dose of $1 \times 10^{15} \text{ Xe}^+/\text{cm}^2$ to $5 \times 10^{15} \text{ Xe}^+/\text{cm}^2$ as shown in Figures 3 and 4, which could confirm the above arguments.

4. Concluding Remarks

(1) On the basis of the design of the interfacial free energy stored in the Ag–Mo multilayered films, the unique amorphous and metastable fcc/bcc SSSS phases in a broad composition range from 25 atom % of Mo to 88 atom % of Mo were obtained in the Ag–Mo system by ion beam mixing.

(2) Atomistic modeling based on an ab initio derived Ag–Mo potential predicts the glass-forming range of the Ag–Mo system to be within a composition range of 10–88 atom % of Mo, which covers and is reasonably broader than the experimentally measured glass-forming range by ion beam mixing.

(3) Molecular dynamics simulations also indicate the possibility of the formation/appearance of a crystalline and amorphous mixture within a narrow composition range from 88 to 92 atom % of Mo, which is fairly compatible with the observed coexisting state that emerged in the $\text{Ag}_{12}\text{Mo}_{88}$ multilayered sample upon ion beam mixing.

Acknowledgment. The authors are grateful to the financial support from the National Natural Science Foundation of China, The Ministry of Science and Technology of China (G20000672), and the Administration of Tsinghua University.

References and Notes

- (1) Klement, W.; Willens, R. H.; Duwez, P. *Nature* **1960**, *187*, 869.
- (2) Zallen, R. *The physics of amorphous solids*; John Wiley & Sons: New York, 1983.
- (3) Greer, A. L. *Science* **1995**, *267*, 1947.
- (4) Lu, Y. Q.; Zhu, Y. Y.; Chen, Y. F.; Zhu, S. N.; Ming, N. B.; Feng, Y. J. *Science* **1999**, *284*, 1822.
- (5) He, J. H.; Ma, E. *Phys. Rev. B* **2001**, *64*, 144206.
- (6) Guo, H. B.; Liu, B. X. *J. Mater. Res.* **2004**, *19*, 1364.
- (7) Cheng, Y.-T.; Van Rossum, M.; Nicolet, M.-A.; Johnson, W. L. *Appl. Phys. Lett.* **1984**, *45*, 185.
- (8) Zhang, Z. J.; Jin, O.; Liu, B. X. *Phys. Rev. B* **1995**, *51*, 8076.
- (9) Zhang, Z. J. Ph.D. Thesis, Tsinghua University, Beijing, China, 1995.
- (10) Li, Z. C.; Yu, D. P.; Liu, B. X. *Phys. Rev. B* **2002**, *65*, 245403.
- (11) Zhang, R. F.; Liu, B. X. *J. Mater. Res.* **2003**, *18*, 1499.
- (12) de Boer, F. R.; Boom, R.; Mattens, W. C. M.; Miedema, A. R.; Niessen, A. K. *Cohesion in metals: Transition metal alloy*; North-Holland: Amsterdam, 1989.
- (13) Ziegler, J. F.; Biersack, J. P. *TRIM*; Pergamon Press: New York, 1992.
- (14) Bakker, H. *Enthalpies in Alloys: Miedema's Semiempirical Model*; Trans Tech: Zurich, Switzerland, 1998.
- (15) Lopez, J. M.; Alonso, J. A. Z. *Naturforsch., A* **1985**, *40*, 1199.
- (16) Alonso, J. A.; Gallego, L. J.; Simozar, J. A. *Nuovo Cimento* **1990**, *12*, 587.
- (17) Zhang, R. F.; Shen, Y. X.; Yan, H. F.; Liu, B. X. *J. Phys. Chem. B* **2005**, *109*, 4391.
- (18) Bakker, H.; Zhou, G. F.; Yang, H. *Prog. Mater. Sci.* **1995**, *39*, 159.
- (19) Miedema, A. R.; den Broeder, F. J. A. Z. *Metallkd.* **1979**, *70*, 14.
- (20) Gerkema, J.; Miedema, A. R. *Surf. Sci.* **1983**, *124*, 351.
- (21) Luzzi, D. E.; Yan, M.; Šob, M.; Vitek, V. *Phys. Rev. Lett.* **1991**, *67*, 1894.
- (22) Yan, M.; Šob, M.; Luzzi, D. E.; Vitek, V.; Ackland, G. J.; Methfessel, M.; Rodriguez, C. O. *Phys. Rev. B* **1993**, *47*, 5571.
- (23) Siegl, R.; Yan, M.; Vitek, V. *Modell. Simul. Mater. Sci. Eng.* **1997**, *5*, 105.
- (24) Kresse, G.; Hafner, J. *Phys. Rev. B* **1993**, *47*, 558.
- (25) Kresse, G.; Furthmüller, J. *Phys. Rev. B* **1996**, *54*, 11169.
- (26) Vanderbilt, D. *Phys. Rev. B* **1990**, *41*, 7892.
- (27) Perdew, J.; Wang, Y. *Phys. Rev. B* **1992**, *45*, 13244.
- (28) Liu, J. B.; Liu, B. X. *Phys. Rev. B* **2001**, *63*, 132204.
- (29) Finnis, M. W.; Sinclair, J. E. *Philos. Mag. A* **1984**, *50*, 45.
- (30) Ackland, G. J.; Tichy, G.; Vitek, V.; Finnis, M. W. *Philos. Mag. A* **1987**, *56*, 735.

- (31) Rebonato, R.; Welch, D. O.; Hatcher, R. D.; Bilello, J. C. *Philos. Mag. A* **1987**, 55, 655.
- (32) Johnson, R. A. *Phys. Rev. B* **1988**, 37, 3924.
- (33) Parrinello, M.; Rahman, A. *J. Appl. Phys.* **1981**, 52, 7182.
- (34) Allen, M. P.; Tildesley, D. J. *Computer Simulation of Liquids*; Clarendon: Oxford, U.K., 1986.
- (35) Ciccotti, G.; Hoover, W. G. *Molecular-Dynamics Simulation of Statistical-Mechanical Systems*; ASI-NATO: North-Holland, The Netherlands, 1986.
- (36) Liu, B. X.; Lai, W. S.; Zhang, Z. J. *Adv. Phys.* **2001**, 50, 367.
- (37) Phillpot, S. R.; Yip, S.; Wolf, D. *Comput. Phys.* **1989**, 3, 20.
- (38) Rosato, V.; Ciccotti, G.; Pontikis, V. *Phys. Rev. B* **1986**, 33, 1860.
- (39) Kittel, C. *Introduction to Solid-State Physics*, 7th ed.; New York, 1996.
- (40) Balluffi, R. W. *J. Nucl. Mater.* **1978**, 69, 70, 240.
- (41) Lide, D. R. *Handbook of Chemistry and Physics*, 81st ed.; CRC press: Boca Raton, FL, 2000–2001.
- (42) Maier, K.; Peo, M.; Saile, B.; Schaefer, H. E.; Seeger, A. *Philos. Mag. A* **1979**, 40, 701.
- (43) Rose, J. H.; Smith, J. R.; Guinea, F.; Ferrante, J. *Phys. Rev. B* **1984**, 29, 2963.
- (44) Li, J. H.; Kong, L. T.; Liu, B. X. *J. Mater. Res.* **2004**, 19, 3547.
- (45) Segall, M. D.; Lindan, P. L.; Probert, M. J.; Pickard, C. J.; Hasnip, P. J.; Clark, S. J.; Payne, M. C. *J. Phys.: Condens. Matter* **2002**, 14, 2717.
- (46) Liu, B. X.; Lai, W. S.; Zhang, Q. *Mater. Sci. Eng., R* **2000**, 29, 1.
- (47) Thompson, M. W. *Defects and radiation damage in metals*; Cambridge University Press: London, 1969.